

Laminar free convection in open-ended vertical 7-rod bundles: numerical

S.C. Haldar *

Department of Mechanical Engineering, Regional Engineering College, Rourkela-769 008, Orissa, India

Abstract

Solely buoyancy induced flow and heat transfer have been investigated numerically in two open-ended 7-rod bundles of differing arrangements. The circular geometry of the six peripheral rods was replaced by equivalent curved trapezium to get rid of non-orthogonal intersections of the grid lines on the rod boundary. Solutions were initiated assuming a value of dimensionless inlet velocity and then progressed longitudinally until the pressure equals that of the ambient. The flat axial velocity profile at inlet gradually changes with the axial distance. The radial velocity profiles show the diminishing entry effects as the flow develops axially. At high heat input, the bundle height is insufficient for the flow to be fully developed. Numerically evaluated volume flow rates are in excellent agreement with the measured values for both the bundles under investigation.

1. Introduction

The need to cool a vertical bank of tubes by pure free convection is sometimes the only option left despite the low rates of heat transfer this mechanism offers.

Buoyancy-induced flow and heat transfer in open-ended vertical geometries like tubes, annuli, parallel plates were studied experimentally and numerically for both isothermal and constant heat flux walls (Bodoia and Osterle, 1962; Davis and Perona, 1971; Dyer, 1975; El-Shaarawi and Sarhan, 1980; Keyhani et al., 1983; Sparrow and Charmchi, 1983; Oosthuizen and Paul, 1986; Al-

Arabi et al., 1987; Rogers and Yao, 1993; Mohanty and Dubey, 1996). Numerical solutions reveal that for the case of isothermal walls, volume flow rate and heat flux have respective maximums if the vertical length of the channel is more than that required for the flow to be fully developed. However, no such maximum exists for channel with constant heat flux walls. This is due to the fact that in an isothermal channel buoyancy force vanishes after the flow becomes fully developed. While in a constant heat flux channel the driving buoyancy force exists throughout the channel height.

In the present paper, numerical results of pure free convection in the same two sets of 7-rod bundles have been reported for which experiments were conducted. The rods were deemed constant

heat flux and the shell adiabatic. The numerical results have been compared with the experiments.

2. Physical model

The 7-rod bundle within a circular shell and the adopted co-ordinate system are depicted in Fig. 1(a). The r, θ grid lines will result in non-ortho-

gonal intersections with the boundaries of each of the six peripheral rods. In order to avoid the associated difficulties, the circular geometry of each of the six peripheral rods has been replaced by equivalent curved trapezoid consisting of two constant- r lines (12 and 43) and two constant- θ lines (14 and 23). The diameter of the outer shell and the spacing between the rods (pitch) were not disturbed.

2.1. Dimensions of the equivalent trapezium

The dimensions of the trapezium, i.e. b^* and ϕ , Fig. 1(a), replacing the circular geometry of the six peripheral rods were chosen by comparing the following two alternatives referred to as model A and B.

2.1.1. Model A

The conditions used in this model are

1. the hydraulic diameter of the actual bundle is equal to that of the approximated bundle, and
2. the sums of the two opposite sides of the trapezium are equal.

These yielded

$$6b^{*2} + 12A_1b^* - (A_2 - A_1A_3) = 0 \quad (1)$$

where $A_1 = (r_2^{*2} - 7)/(r_2^{*2} + 7)$, $A_2 = \pi(r_2^{*2} - 1)$ and $A_3 = \pi(r_2^{*2} + 1)$ and

$$\phi = b^*/P^* \quad (2)$$

Solution of Eqs. (1) and (2) for b^* and ϕ determines the size of the trapezium.

2.1.2. Model B

The two conditions in the second alternative are

1. the circular rod area and the trapezium area are equal, and
2. the error in perimeter between the circular geometry and the trapezium is minimum resulting in

$$\phi = \sqrt{\pi}/P^* \quad (3)$$

$$\text{and } b^* = \sqrt{\pi}. \quad (4)$$

In contrast to model A, we find here that the dimensionless height of the trapezium, b^* , has no reference to the pitch. Intuitively, model A ap-

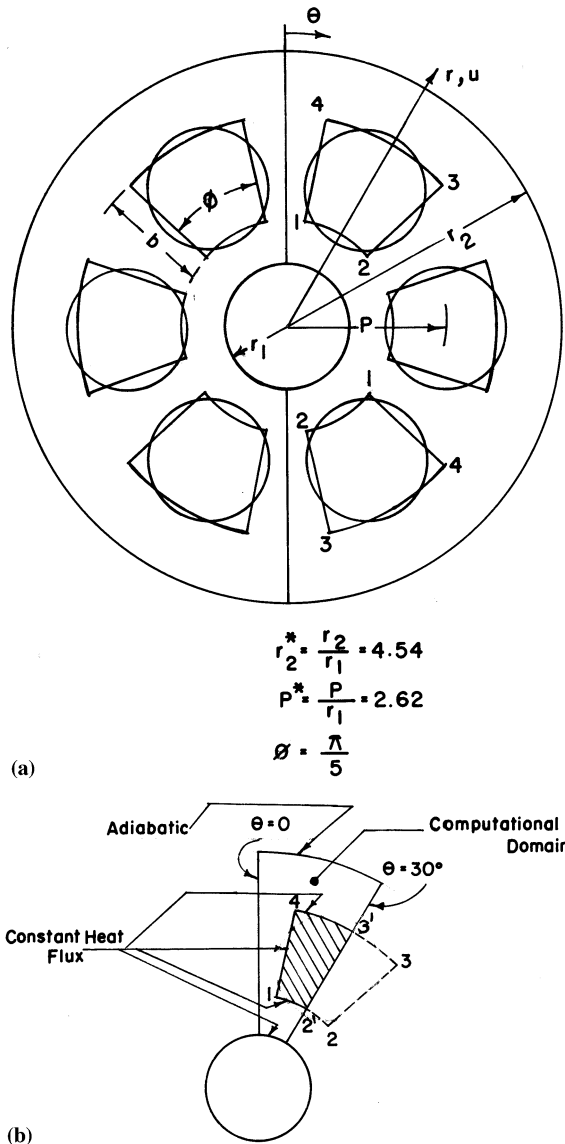


Fig. 1. (a) Schematic diagram of the physical model, (b) computational domain; 30° symmetry sector.

pears to be more general, for it accounts for the rod arrangement. We checked the suitability of the two models by comparing the bundle average fRe and Nu values under forced convection condition with the available literature information (Benodekar and Date, 1978; Das and Mohanty, 1984) and the model A was found to be marginally superior.

3. Mathematical formulation

The heated vertical rods produce a free convective flow entering the bundle at the bottom and leaving at the top. The governing equations for steady, laminar free convection flow with Boussinesq's assumption are well known. The equations were non-dimensionalised by introducing the dimensionless variables as defined in the nomenclature and the non-dimensionalised equations are:

continuity:

$$\frac{\partial w^*}{\partial z^*} + \frac{1}{r^*} \frac{\partial(u^* r^*)}{\partial r^*} = 0 \quad (5)$$

axial momentum:

$$w^* \frac{\partial w^*}{\partial z^*} + u^* \frac{\partial w^*}{\partial r^*} = -\frac{dp^*}{dz^*} + \frac{1}{r^*} \frac{\partial}{\partial r^*} \left(r^* \frac{\partial w^*}{\partial r^*} \right) + T^* \quad (6)$$

energy:

$$w^* \frac{\partial T^*}{\partial z^*} + u^* \frac{\partial T^*}{\partial r^*} = \frac{1}{Pr} \frac{1}{r^*} \frac{\partial}{\partial r^*} \left(r^* \frac{\partial T^*}{\partial r^*} \right) \quad (7)$$

where the pressure defect p' as defined by Bodoia and Osterle (1962) is given by

$$p'(z) = p(z) - (p_0 - \rho_0 g z). \quad (8)$$

3.1. Boundary conditions

Computations were performed on a 30° symmetry sector as shown in Fig. 1(b) with the following conditions on the solid boundaries and the symmetry planes.

3.1.1. Central rod and outer shell

1. No slip on these surfaces yields $w^* = u^* = 0$ at all θ on $r^* = 1$ and r_2^* .

2. Uniform heat flux on the central rod can be expressed as

$$q = -k \frac{\partial T}{\partial r} \quad \text{on } r = r_1$$

which after non-dimensionalization becomes

$$\frac{\partial T^*}{\partial r^*} = -1 \quad \text{on } r^* = 1.$$

The adiabatic condition on the shell reduces to

$$\frac{\partial T^*}{\partial r^*} = 0 \quad \text{on } r^* = r_2^*.$$

3.1.2. Symmetry planes

The conditions on the two planes of symmetry are written as

- (i) $\frac{\partial w^*}{\partial \theta} = \frac{\partial u^*}{\partial \theta} = 0$ at all r^* on $\theta = 0$ and 30° .

Also,

- (ii) $\frac{\partial T^*}{\partial \theta} = 0$ at all r^* on $\theta = 0$ and 30° .

3.1.3. Peripheral rod

1. No slip conditions, $w^* = u^* = 0$, apply on the solid surfaces 12', 14 and 43'; Fig. 1(b).

2. $\frac{\partial T^*}{\partial \theta} = +1$ on the surface 14 along the -ve θ -direction.

$$\frac{\partial T^*}{\partial r^*} = +1 \quad \text{on the surface 12' along the}$$

-ve r -direction.

= -1 on the surface 43' along the +ve r -direction.

3.1.4. Inlet

The uniform inlet velocity at ambient temperature is expressed symbolically as

1. $w^* = w_0^*$ at $z^* = 0$ for all r^* and θ .
2. $T^* = 0$ at $z^* = 0$ for all r^* and θ .
3. Application of Bernoulli's equation between the inlet to the bundle and a far-off point in the ambient at the same elevation results $p'^* = -w_0^{*2}/2$ at $z^* = 0$.

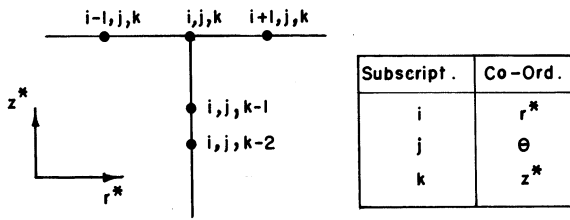


Fig. 2. Grid system at a particular angle.

It may be mentioned here that in the early works by Bodoia and Osterle (1962) and Davis and Perona (1971), the pressure defect p' at inlet to the bundle was assumed zero.

3.1.5. Exit

The ambient pressure at the exit to the bundle is written as

1. $p'^* = 0$ at $z^* = L^*$ where L^* is the dimensionless height of the bundle.

4. Solution

The governing equations together with the above specified boundary conditions were solved by finite difference method using successive over relaxation (SOR) technique for two 7-rod bundles; one with $r_2^* = 4.54$ and $P^* = 2.62$, referred to as bundle # 1 and the other with $r_2^* = 5.3$ and $P^* = 2.53$, referred to as bundle # 2. The salient features of the numerical method are enumerated below.

1. The momentum and energy equations are parabolic in nature facilitating a marching procedure from the bottom to the top of the bundle and accordingly, the differentials w.r.t. z^* , except the term dp'^*/dz^* in Eq. (6), were expressed by three point backward difference scheme with non-uniform spacings. However, the central difference was adopted for the differentials w.r.t. r^* except the term $\partial(u^*r^*)/\partial r^*$ in the continuity equation. The associated grid system at a particular angular position is shown in Fig. 2.
2. The scheme adopted to evaluate u^* from continuity equation is quite different from that reported in the literature (Bodoia and Osterle, 1962; Al-Arabi et al., 1987; Mohanty and

Dubey, 1996) and needs to be elaborated. Expressing the term (u^*r^*) at (i, j, k) about $(i-1, j, k)$, and about $(i+1, j, k)$ by Taylor's series without the higher order terms, we get,

$$(u^*r^*)_{i,j,k} = (u^*r^*)_{i-1,j,k} + \left. \frac{\partial(u^*r^*)}{\partial r^*} \right|_{i-1,j,k} \cdot \Delta r^*$$

$$(u^*r^*)_{i,j,k} = (u^*r^*)_{i+1,j,k} - \left. \frac{\partial(u^*r^*)}{\partial r^*} \right|_{i+1,j,k} \cdot \Delta r^*.$$

Adding, $2(u^*r^*)_{i,j,k}$

$$= (u^*r^*)_{i-1,j,k} + (u^*r^*)_{i+1,j,k} - r^* \left. \frac{\partial w^*}{\partial z^*} \right|_{i-1,j,k} \cdot \Delta r^* + r^* \left. \frac{\partial w^*}{\partial z^*} \right|_{i+1,j,k} \cdot \Delta r^* \quad (9)$$

since $\frac{\partial(u^*r^*)}{\partial r^*} = -r^* \frac{\partial w^*}{\partial z^*}$ from Eq. (5).

The RHS of Eq. (9) was assumed known from the previous iteration and then u^* was evaluated by an iterative technique.

3. The temperatures on the solid surfaces as well as the symmetry planes were determined by the three point one-sided difference scheme satisfying the respective thermal boundary conditions.
4. The term dp'^*/dz^* in Eq. (6) was calculated following the procedure described by Patankar and Spalding (1972).
5. A grid independence test was performed to arrive at a suitable grid size of $\approx 50 \times 30$ in the r and θ directions, respectively.
6. The computation was commenced by assuming a value of w_0^* , the dimensionless inlet velocity. The solution was then marched in the +ve z^* direction until the pressure defect, p'^* becomes zero. The corresponding z^* , denoted by L^* , is the dimensionless height of the bundle required to induce the assumed flow of w_0^* .
7. The axial spacing at inlet (Δz^*) was varied between 10^{-7} and 10^{-4} depending on the value of w_0^* and the subsequent Δz^* was increased to 1.1 times the previous value up to a specified maximum. However, the uniform spacings were preferred along r - and θ -directions.

8. All the equations were deemed converged when the difference between two consecutive iterations is $< 0.001\%$ at all the nodes. The global convergence was performed till the values of T^* and w^* at all the node points were $< 0.0001\%$ between two consecutive cycles, where one cycle consists of solutions of Eq. (5) for u^* , Eq. (6) for w^* and dp^*/dz^* , and Eq. (7) for T^* .

5. Results and discussions

The numerical results were generated for two sets of 7-rod bundles within circular shell having different arrangements and for various w_0^* . However, the discussions concentrate mainly on the bundle with $r_2^* = 4.54$ and $P^* = 2.62$, bundle # 1, and these apply to the other bundle too. The rods were assumed circumferentially and longitudinally under uniform heat flux condition and the shell adiabatic. Air was chosen as the working medium by specifying a Pr value of 0.7. The numerically determined Nusselt numbers and volume flow rates at inlet to each of the bundles have been compared with those obtained from the experiments, the details of which have been described in the previous paper.

5.1. Axial velocity

Axial velocity profiles at various z^* for $\theta = 0$ and 30° have been plotted in Fig. 3(a) and (b) for $w_0^* = 0.5$ and in Fig. 4(a) and (b) for $w_0^* = 0.01$. The dimensionless inlet velocity, w_0^* is inversely proportional to the Grashof number since the reference axial velocity was chosen as $(v_0/r_1)Gr$. At higher w_0^* and consequently lower Gr, the flat inlet profile changes as the flow progresses axially. The profiles at $\theta = 0$ now have two peaks; the smaller one close to the central rod and the bigger one close to the outer shell, Fig. 3(a). With increasing z^* , the average axial velocity at $\theta = 0$ increases and that at $\theta = 30^\circ$ decreases such that the overall continuity is maintained.

The profiles for higher Gr or lower w_0^* show a different trend, Fig. 4(a) and (b). At $\theta = 0$, the peaks shift towards the central rod with increasing

axial distance as is observed in annular geometry (Al-Arabi et al., 1987). The flow even reverses near the outer shell, Fig. 4(a).

5.2. Radial velocity

The radial velocity profiles at the identical axial and angular positions and for the same w_0^* of 0.5 and 0.01 are presented in Fig. 5(a),(b) and 6(a),(b), respectively. The profiles for $w_0^* = 0.5$ have a positive loop followed by a negative loop. This is due to the fact that at entry to the bundle the streamlines move away from the walls resulting a +ve radial velocity component near the walls facing the +ve r -direction (central rod and the surface 43') and a -ve component near the walls facing the -ve r -direction (shell and the surface 12', Fig. 1). The flow becomes hydrodynamically fully developed as reflected by zero radial velocity component at $z^* = 2.75$ for $\theta = 0$ and at $z^* = 0.1164$ for $\theta = 30^\circ$. The less flow area due to presence of a peripheral rod at $\theta = 30^\circ$ causes a faster flow development there.

The profiles at high heat input, i.e. $w_0^* = 0.01$, Fig. 6(a) and (b), take a different shape which may be explained by the fact that there are two effects in the developing flow field: entry and buoyancy. The profile at $z^* = 0.1779 \times 10^{-3}$ is primarily due to a strong entry effects. With increasing z^* , entry effect diminishes and consequently buoyancy becomes stronger and the fluid moves towards the central rod resulting in -ve radial velocity component, Fig. 6(a).

The non-zero u^* at the exit to the bundle, i.e. at $z^* = 0.2922 \times 10^{-2}$, Fig. 6(a), implies that the flow has not reached its fully developed condition before leaving the bundle. The faster development at $\theta = 30^\circ$ plane results in almost zero radial velocity at the same z^* of 0.2922×10^{-2} , Fig. 6(b).

5.3. Temperature

Fig. 7(a) and (b) plot the temperature profiles at different axial locations for $w_0^* = 0.5$ and Fig. 8(a) and (b) for $w_0^* = 0.01$ for the same two angular positions of 0 and 30° . At $w_0^* = 0.5$, the profiles are nearly straight due to weak buoyancy

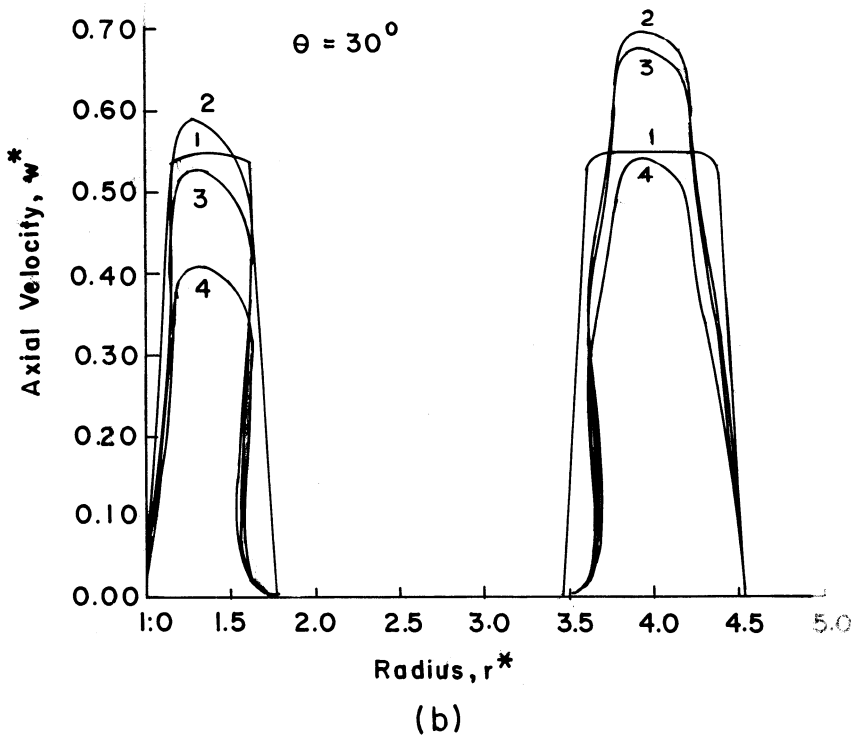
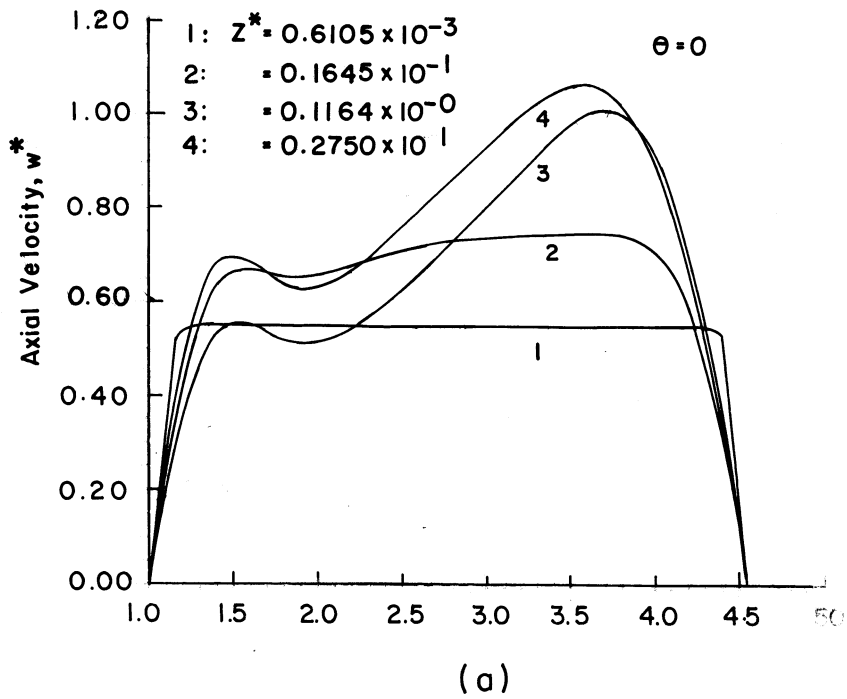


Fig. 3. (a), (b) Development of axial velocity, $w_0^* = 0.50$.

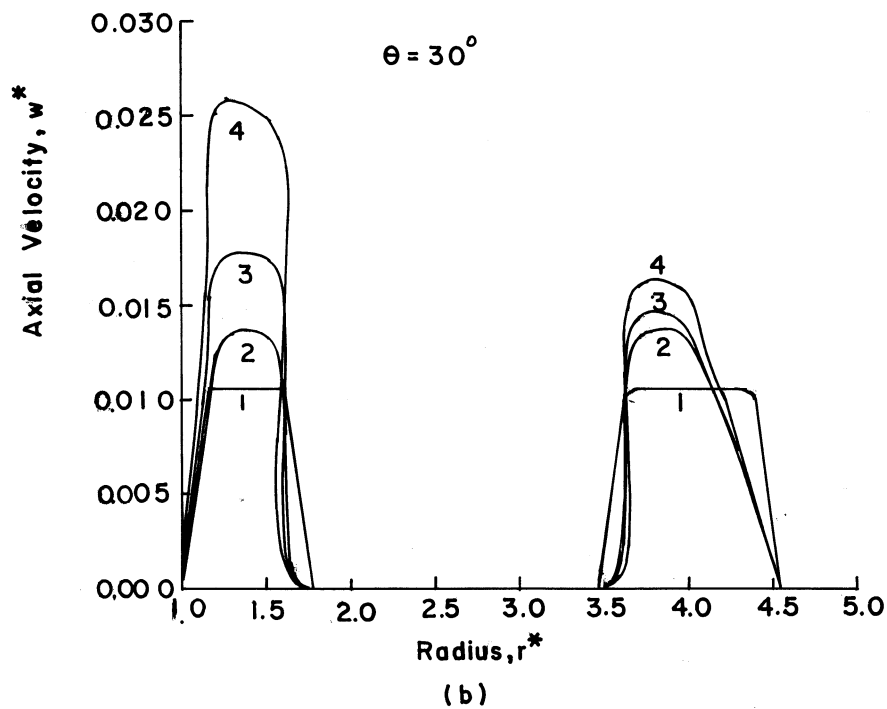
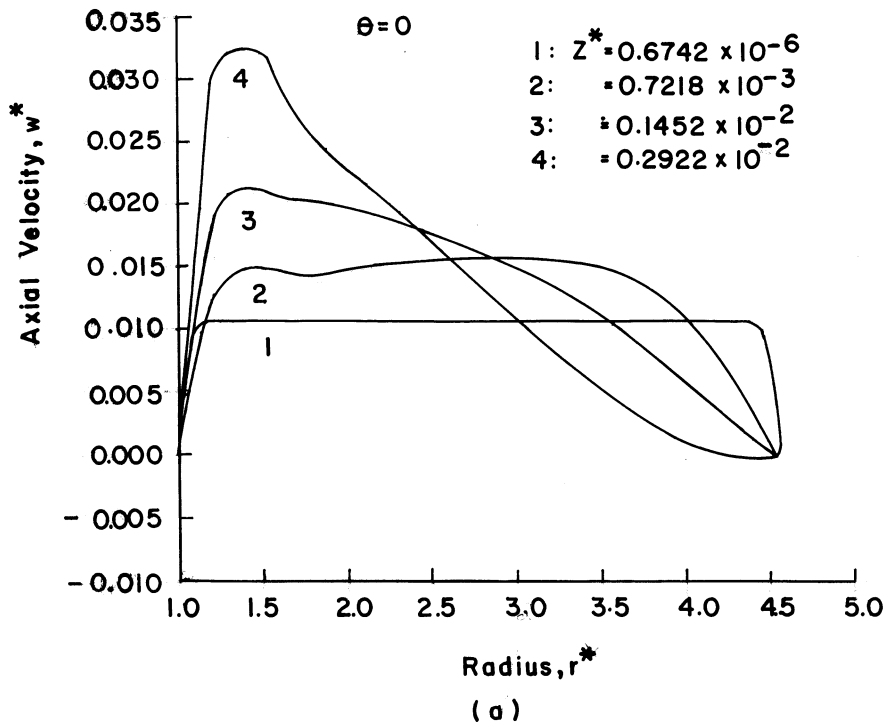


Fig. 4. (a), (b) Development of axial velocity, $w_0^* = 0.01$.

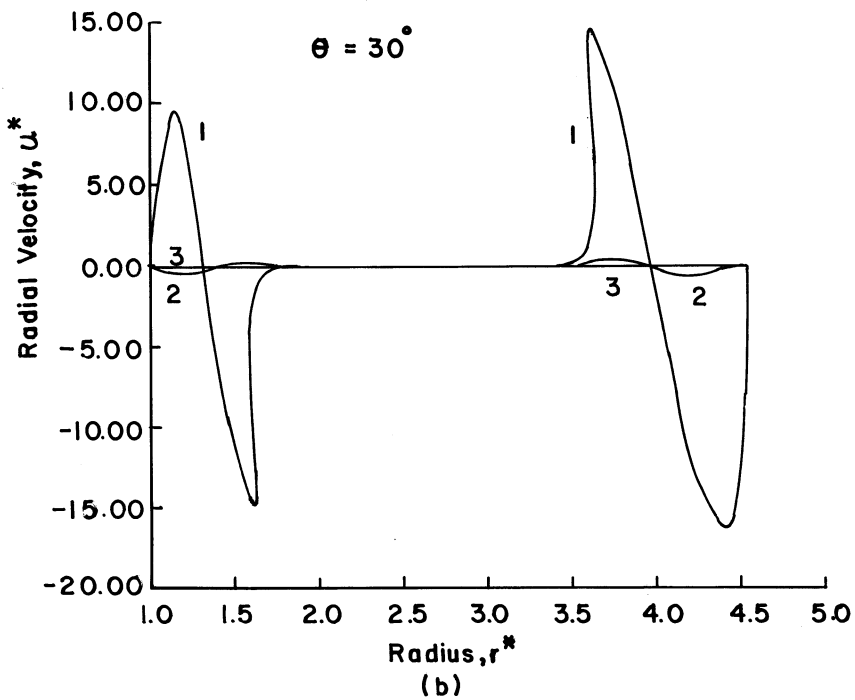
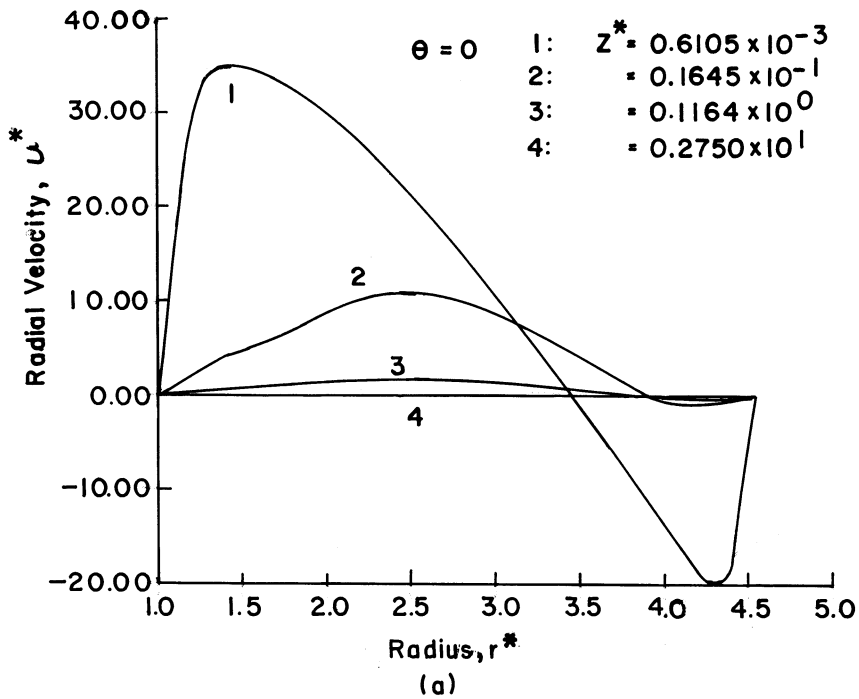


Fig. 5. 7(a), (b) Longitudinal variation of radial velocity profiles, $w_0^* = 0.50$.

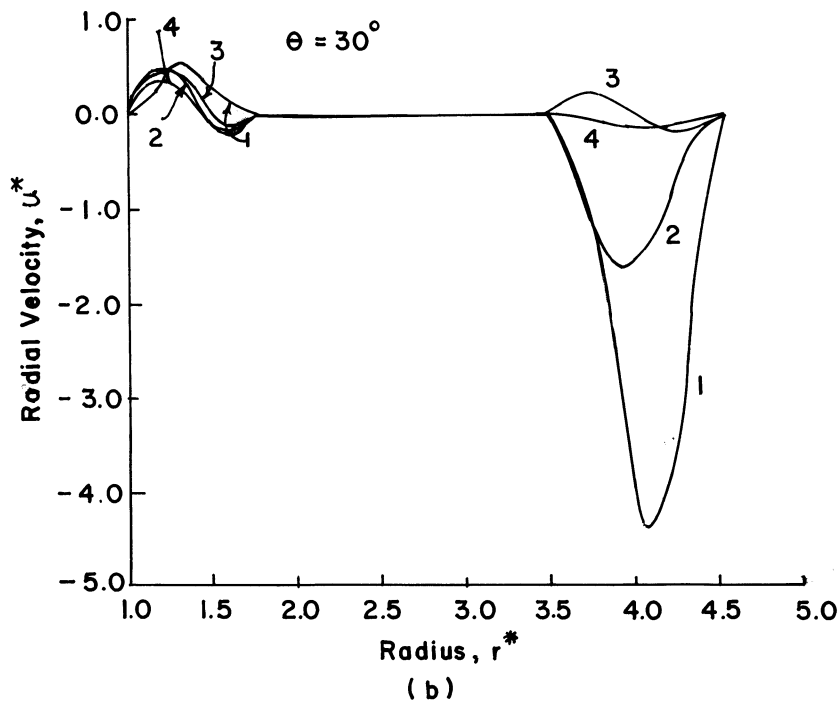
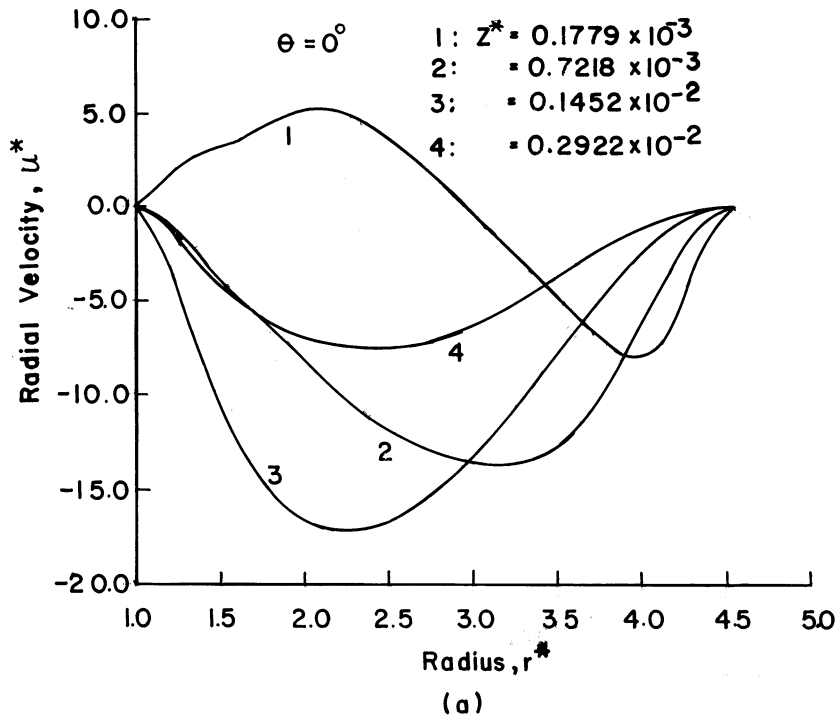


Fig. 6. (a), (b) Longitudinal variation of radial velocity profiles, $w_0^* = 0.01$.

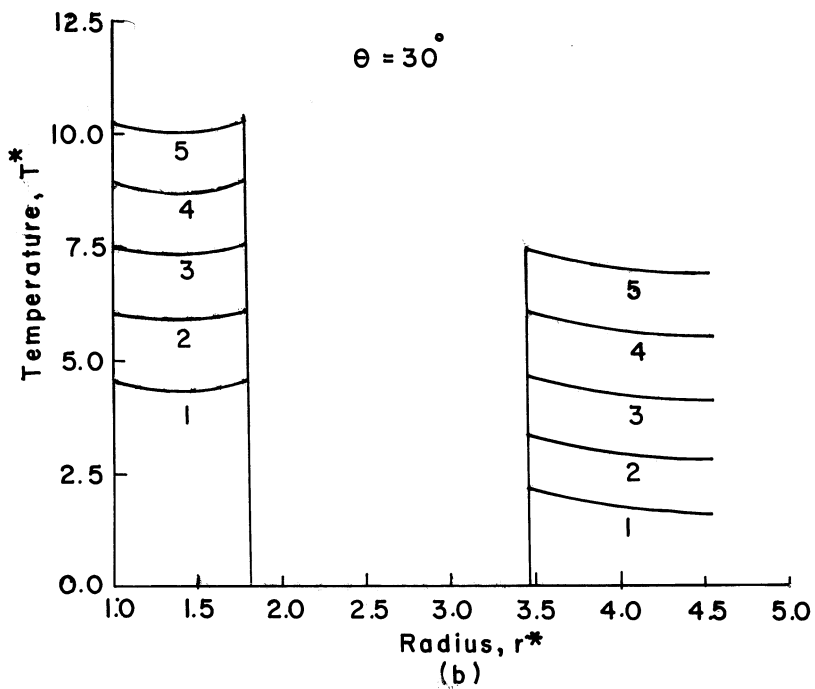
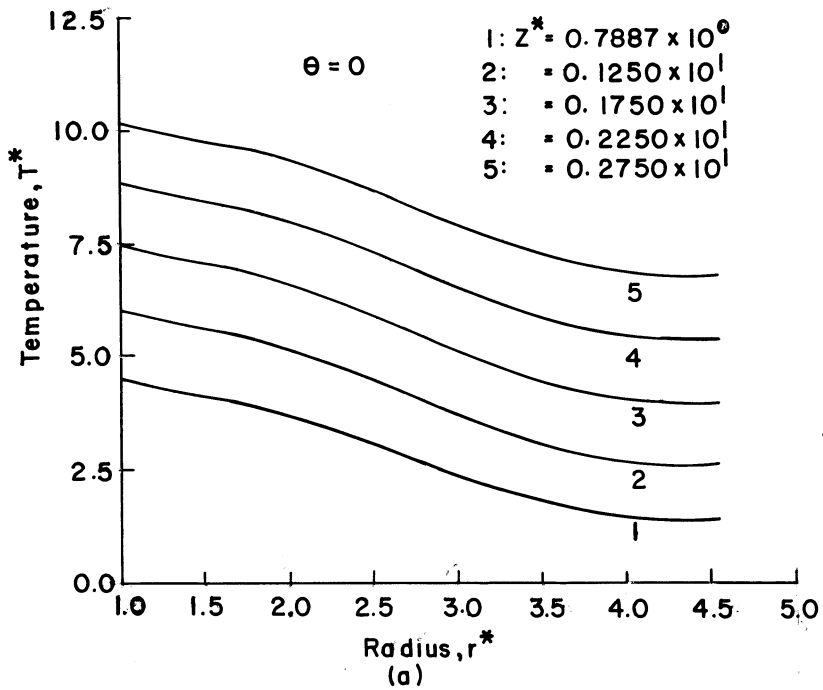


Fig. 7. (a), (b) Axial development of temperature profiles, $w_0^* = 0.50$.

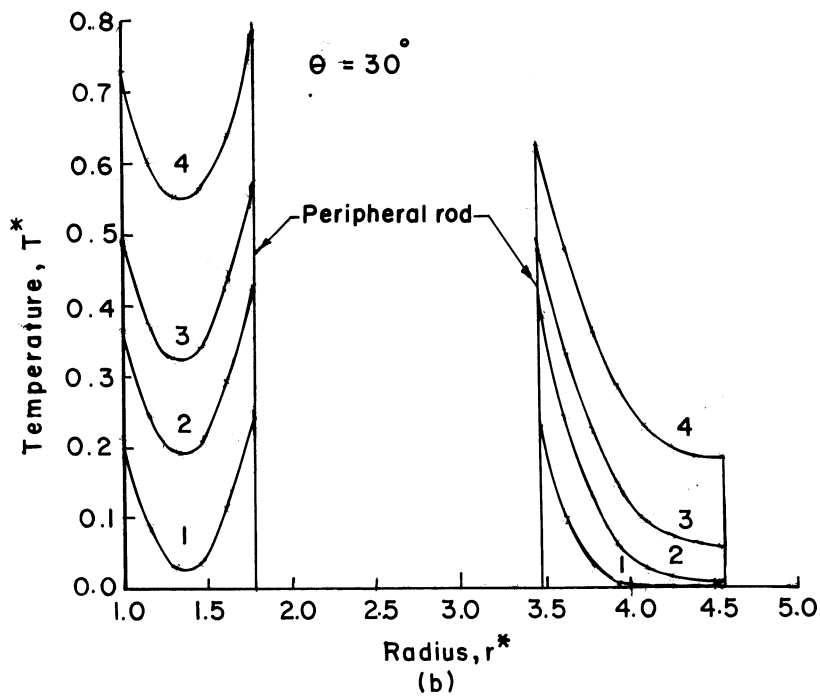
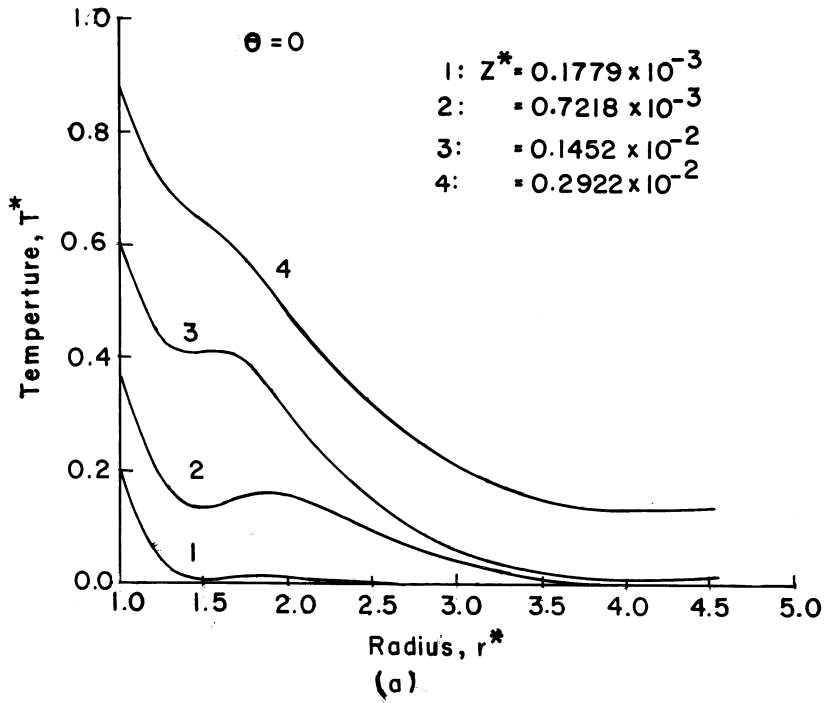


Fig. 8. (a), (b) Axial development of temperature profiles, $w_0^* = 0.01$.

effect while the curved profiles at $w_0^* = 0.01$ are due to a stronger buoyancy effect. The constant heat flux on the rods and the adiabatic condition on the shell may be noted from the figures.

The axial variation of the central rod average temperature, the peripheral rod average temperature and the fluid bulk temperature are shown in Fig. 9. The higher temperature of the central rod over the peripheral rods is obviously due to its position in the bundle and all of them increase monotonically because of the uniform heat flux condition axially and peripherally.

5.4. Nusselt number

The bundle average Nusselt number based on hydraulic diameter was determined from $\overline{Nu}_{D_h} = D_h^*(\overline{T}_w^* - T_b^*)$.

As expected, the Nusselt number decreases monotonically with increasing axial distance. The fully developed condition at the exit to the bundle for $w_0^* = 0.5$ may be seen from Fig. 10(a), while the plot for $w_0^* = 0.01$, Fig. 10(b), corroborates our earlier inference of developing flow at the bundle exit.

Numerically determined Nusselt numbers of central and peripheral rods, averaged circumfer-

entially and longitudinally have been presented in Fig. 11(a) for bundle # 1 as a function of dimensionless bundle height and in Fig. 11(b) for bundle # 2. The experimental values have been plotted therein for comparison. Due to its position in a bundle, the central rod will have higher surface temperature and consequently lower Nusselt number than those for the peripheral rods. The difference in Nusselt number between central and peripheral rods obtained from numerical solution is larger than what has been observed experimentally, specially so for bundle # 1. In case of bundle # 2, the agreement between the experimental and numerical Nusselt numbers of the peripheral rods is quite satisfactory while for the central rod the measured values are slightly higher than the corresponding numerical values, Fig. 11(b). For bundle # 1, the measured Nusselt numbers of the central rod are in excellent agreement with those obtained from the numerical solution, Fig. 11(a), but the measured Nu of the peripheral rods are marginally higher than the respective values for the central rod and significantly lower than the corresponding numerical results, Fig. 11(a).

The Nusselt number values averaged over all the seven rods, Fig. 12, are very close to those for the peripheral rods as there are six peripheral rods against one central rod in a bundle of seven rods. The good agreement for bundle # 2 and the large deviation for bundle # 1 are obvious in the light of the above discussions.

5.5. Pressure defect

Application of Bernoulli's equation yields $p'^* = -w_0^{*2}/2$ at inlet to the bundle. The solution was then progressed longitudinally until zero pressure defect was encountered establishing the bundle height required to ingress a flow of w_0^* . So a negative pressure defect exists throughout the bundle length, Fig. 13, implying that the static pressure in the bundle is always less than the ambient pressure at that elevation, Eq. (8). It may also be noted from the figure that the minimum pressure occurs near the middle of the bundle.

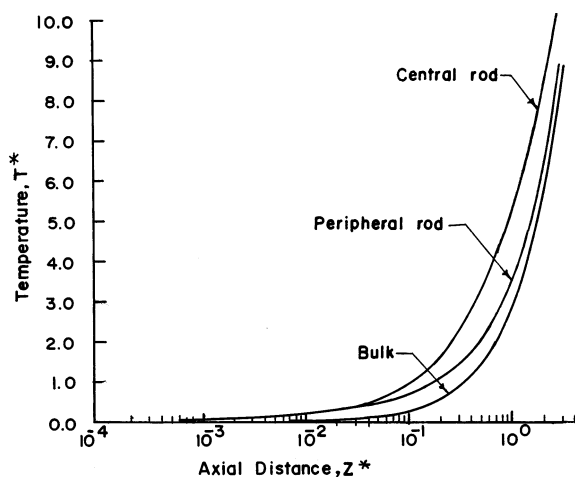
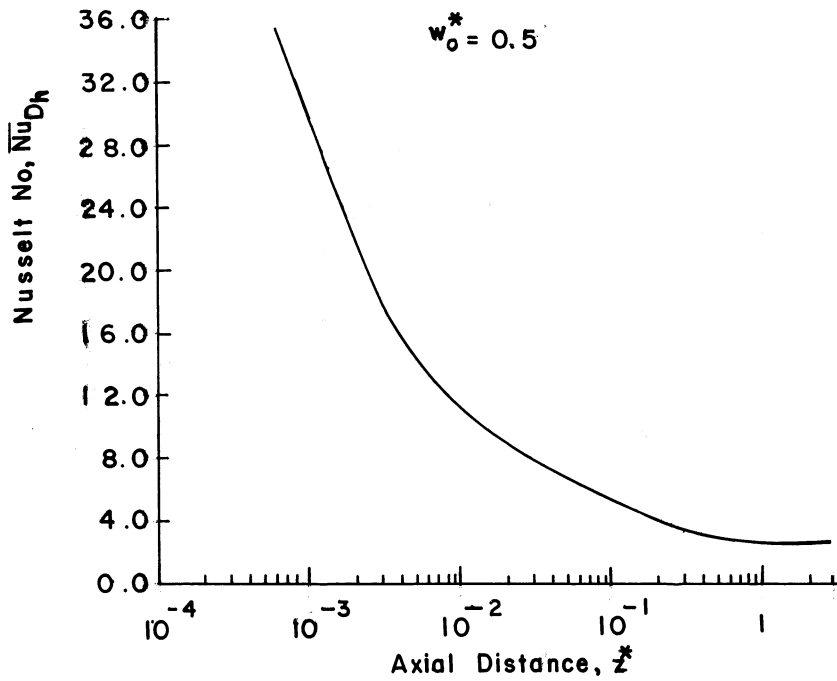
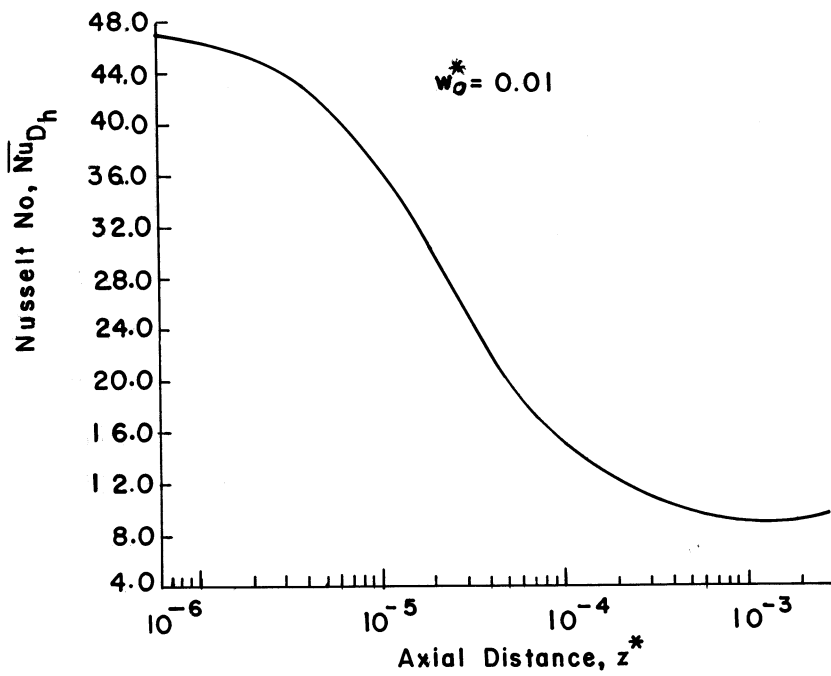


Fig. 9. Axial variation of rod surface temperature and bulk temperature, $w_0^* = 0.50$.



(a)



(b)

Fig. 10. (a), (b) Change of Nusselt number with axial distance.

5.6. Volume flow rate

Fig. 14 presents the numerical and experimental variations of Q_0^* with L^* for both the bundles under investigation. Experimentally the volume flow rates were measured by a TSI 1050 hot wire anemometry, the details of which have been reported in the previous paper. The close agreement between the numerical and experimental results validate the simplifications adopted to carry out the numerical solution.

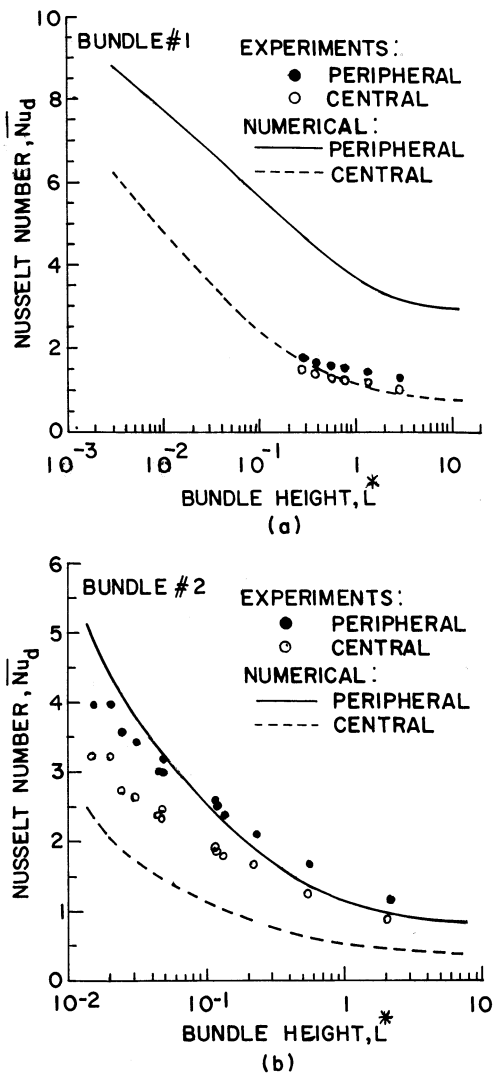


Fig. 11. (a), (b) Average Nusselt number of central and peripheral rods; comparison with experiments.

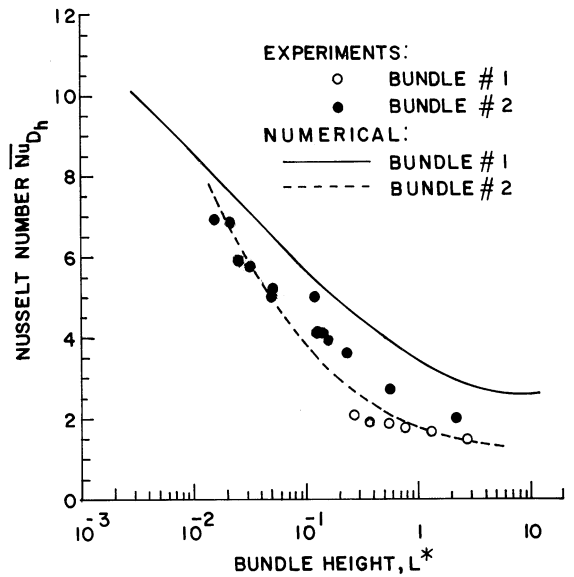


Fig. 12. Dimensionless bundle height vs. Nusselt number; comparison with experiments.

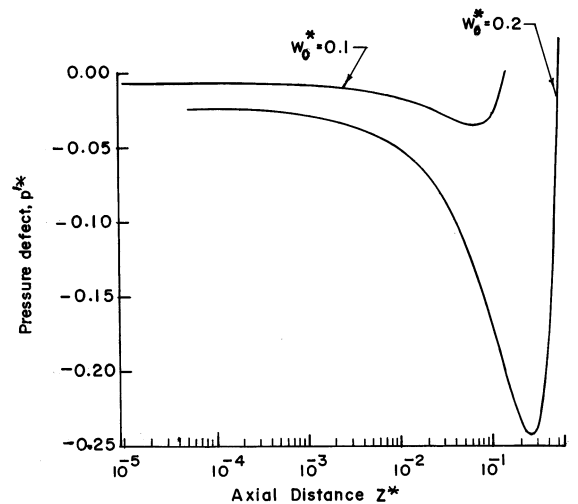


Fig. 13. Variation of pressure defect with axial distance.

Appendix A. Nomenclature

Symbol	Description
--------	-------------

English symbols

b	radial length of the trapezium (m), Fig. 1(a); $b^* = b/r_1$
-----	--

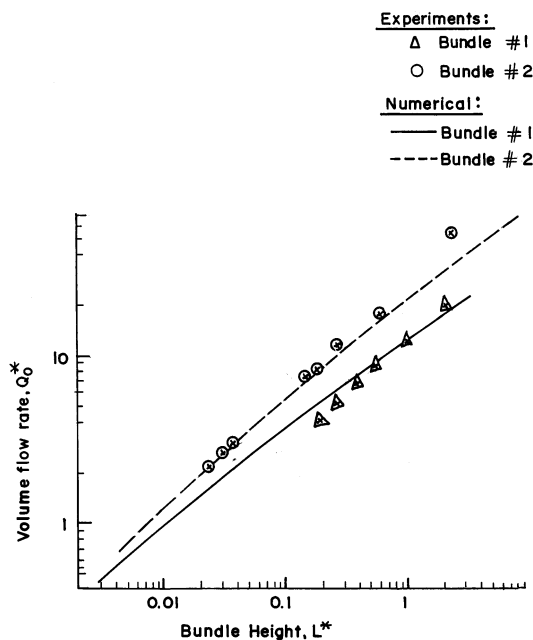


Fig. 14. Dimensionless bundle length vs. dimensionless volume flow rate; comparison with experiments.

d	rod diameter (m)
D_h	bundle hydraulic diameter (m); $D_h^* = D_h/r_1$
g	acceleration due to gravity (m s^{-2})
Gr	Grashof number, $Gr = g\beta qr_1^4 / (k\nu^2)$
\bar{h}	convective heat transfer coefficient averaged over the desired surface ($\text{W m}^{-2} \text{K}^{-1}$)
k	fluid thermal conductivity ($\text{W m}^{-1} \text{K}^{-1}$)
L	bundle height (m); $L^* = L / (r_1 Gr)$
\overline{Nu}_{D_h}	average Nusselt number, $\overline{Nu}_{D_h} = \bar{h} D_h^* / k = D_h / (\bar{T}_w^* - T_b^*)$
\overline{Nu}_d	average Nusselt number, $\overline{Nu}_d = \bar{h} d / k = 2 / (\bar{T}_w^* - T_b^*)$
p	static pressure (N m^{-2})
p'	pressure defect (N m^{-2}), Eq. (8); $p'^* = p' / (\rho w_{\text{ref}}^2)$
Pr	Prandtl number
Q	volume flow rate ($\text{m}^3 \text{s}^{-1}$); $Q^* = Q / (r_1^2 w_{\text{ref}})$

q	heat flux (W m^{-2})
r	radial co-ordinate (m); $r^* = r/r_1$
r_1	rod radius (m)
r_2	shell radius (m)
T	temperature (K); $T^* = (T - T_0) / T_{\text{ref}}$
T_b	fluid bulk temperature (K); $T_b^* = (T_b - T_0) / T_{\text{ref}}$
T_{ref}	reference temperature (K), $T_{\text{ref}} = qr_1 / k$
\bar{T}_w	temperature of averaging surface (K); $\bar{T}_w^* = (\bar{T}_w - T_0) / T_{\text{ref}}$
u	radial velocity (m s^{-1}); $u^* = u / (v_0 / r_1)$
w	axial velocity (m s^{-1}); $w^* = w / w_{\text{ref}}$
w_{ref}	reference axial velocity (m s^{-1}), $w_{\text{ref}} = (v_0 / r_1) Gr$
z	axial co-ordinate (m); $z^* = z / (r_1 Gr)$

Greek symbols

β	volumetric coefficient of thermal expansion (K^{-1})
θ	angular co-ordinate
ϕ	included angle of the trapezium, Fig. 1(a)
ρ	fluid density (kg m^{-3})
ν	kinematic viscosity ($\text{m}^2 \text{s}^{-1}$)

Subscripts

0	inlet condition
---	-----------------

Superscripts

*	dimensionless quantity
---	------------------------

References

- Al-Arabi, M., El-shaarawi, M.A.I., Khamis, M., 1987. Natural convection in uniformly heated vertical annuli. *Int. J. Heat Mass Transf.* 30, 1381–1389.
- Benodekar, R.W., Date, A.W., 1978. Numerical prediction of heat transfer characteristics of fully developed laminar flow through a circular channel containing rod clusters. *Int. J. Heat Mass Transf.* 21, 935–945.
- Bodoia, J.R., Osterle, J.F., 1962. The development of free convection between heated vertical plates. *Trans. ASME J. Heat Transf.* 84, 40–44.

- Das, R., Mohanty, A.K., 1984. Laminar combined convection in finite circular rod bundles. *Trans. ASME J. Heat Transf.* 106, 563–569.
- Davis, L.P., Perona, J.J., 1971. Development of free convection flow of a gas in a heated vertical open tube. *Int. J. Heat Mass Transf.* 14, 889–903.
- Dyer, J.R., 1975. The development of laminar natural convective flow in a vertical uniform heat flux duct. *Int. J. Heat Mass Transf.* 18, 1455–1465.
- El-Shaarawi, M.A.I., Sarhan, A., 1980. Free convection effects on the developing laminar flow in vertical concentric annulus. *Trans. ASME J. Heat Transf.* 102, 617–622.
- Keyhani, M., Kulacki, F.A., Christensen, R.N., 1983. Free convection in a vertical annulus with constant heat flux on the inner wall. *Trans. ASME J. Heat Transf.* 105, 454–459.
- Mohanty, A.K., Dubey, M.R., 1996. Buoyancy induced flow and heat transfer through a vertical annulus. *Int. J. Heat Mass Transf.* 39, 2087–2093.
- Oosthuizen, P.H., Paul, J.T., 1986. A numerical study of free convective flow through a vertical annular duct, Winter Annual Meeting, ASME, Anaheim, CA.
- Patankar, S.V., Spalding, D.B., 1972. Calculation procedure for heat, mass and momentum transfer in three dimensional parabolic flows. *Int. J. Heat Mass Transf.* 15, 1787–1806.
- Rogers, B.B., Yao, L.S., 1993. Natural convection in a heated annulus. *Int. J. Heat Mass Transf.* 36, 35–47.
- Sparrow, E.M., Charmchi, M., 1983. Natural convection experiments in an enclosure between eccentric or concentric vertical cylinders of different height and diameter. *Int. J. Heat Mass Transf.* 26, 133–143.